A FEASIBILITY STUDY ON GUIDED WAVE-BASED ROBOTIC MAPPING

Morteza Tabatabaeipour
Department of Electronic &
Electrical Engineering
University of Strathclyde
Glasgow, UK
Morteza.tabatabaeipour@strath.a
c.uk

Oksana Trushkevych
Department of physics
University of Warwick
Coventry, UK
O.Trushkevych@warwick.ac.uk

Gordon Dobie
Department of Electronic &
Electrical Engineering
University of Strathclyde
Glasgow, UK
gordon.dobie@strath.ac.uk

Rachel S. Edwards
Department of physics
University of Warwick
Coventry, UK
R.S.Edwards@warwick.ac.uk

Steven Dixon
Department of physics
University of Warwick
Coventry, UK
S.M.Dixon@warwick.ac.uk

Charles MacLeod
Department of Electronic &
Electrical Engineering
University of Strathclyde
Glasgow, UK
charles.macleod@strath.ac.uk

Anthony Gachagan
Department of Electronic &
Electrical Engineering
University of Strathclyde
Glasgow, UK
a.gachagan@strath.ac.uk

S. Gareth Pierce
Department of Electronic &
Electrical Engineering
University of Strathclyde
Glasgow, UK
s.g.pierce@strath.ac.uk

Abstract— **Ultrasonic guided wave imaging techniques have received much attention in recent years for fast screening of large structures. Here we explore the feasibility of Occupancy Grid Mapping (OGM) in order to construct a map of an unknown component for inspection. OGM is a well-established algorithm in robotics, but for the first time we are applying it to Shear Horizontal (SH) guided wave imaging. This approach, in contrast to some existing guided wave-based imaging techniques, would not require prior knowledge of an intact state of the sample. OGM works on the ranges obtained by the Time of Flight (ToF) of the received signals operating in pseudo-pulse-echo mode.**

Keywords—ultrasonic inspection, EMAT, robotic mapping, occupancy grid mapping, SH guided waves

I. INTRODUCTION

Manual NDE inspection can be slow, expensive and potentially hazardous to an operator, such as when performing NDE inspection of high-radiation areas of nuclear power stations. In contrast, automated inspection can be cheaper, safer and more accurate [1]. However, the state of the art robotic inspection scans maximise coverage across the component surface using conventional ultrasonic transducers (including wheel probes), limiting their application for automated in-service inspection.

One commercial example of an automated ultrasonic inspection is the Scorpion series from Silverwing, see Fig. 1 [2]. The current state-of-the-art robotic inspection systems are usually equipped with water and/or dry coupled ultrasonic transducers. Therefore, there are some inherent limitations with the current version of the system. For instance, the surface to be inspected must have a surface temperature of no greater than 80°C, and it must be free of excess rust and scale [3]. Therefore, we propose to take advantage of electromagnetic acoustic transducers (EMATs) with the capability of measuring signals at high temperatures [4]. Moreover, there is no need to remove external scale from the component surface for EMAT inspection and the transducer can be used at a small stand-off distance from the surface.

The current state-of-the-art robotic crawler does inspection by measuring A-scan signals point by point, which is time-consuming and limiting for the inspection of inaccessible areas. Therefore, the authors of this paper have put forward the use of guided waves with the capability of close, mid and long-range ultrasonic inspection.

In summary, the aim of the current study is to use robot mounted EMATs, generating guided waves (e.g. Shear Horizontal (SH) guided waves) to consider an intelligent closed-loop NDE in which the robot paths are based on a) intelligently mapping the structure's geometry while highlighting the areas of significant wall loss, see Fig. 2, and b) an automated interpretation of NDE data where the robot focuses on the regions of concern in more detail.

A. Shear Horizontal Guided Waves

Shear Horizontal (SH) guided waves oscillate perpendicular to the propagation path with a polarization parallel to the surface of the material. SH waves can be generated by EMATs and are increasingly used for the NDT examination of both plate and pipe structures [5] as SH waves scatter from both perpendicular and parallel defects relative to the wave front. Furthermore, it has been reported that SH_1 wave modes are sensitive to wall thinning damage due to the dispersive behaviour of this mode [6].
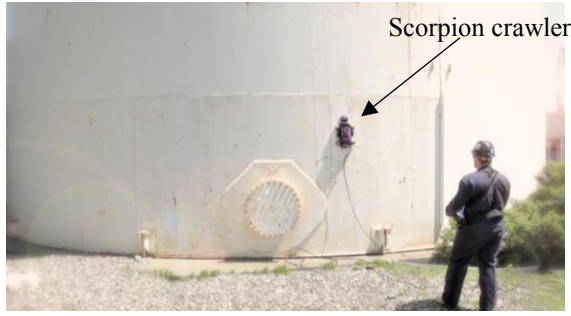
Fig. 1. Ultrasonic tank shell inspection using a Scorpion remote crawler [2].
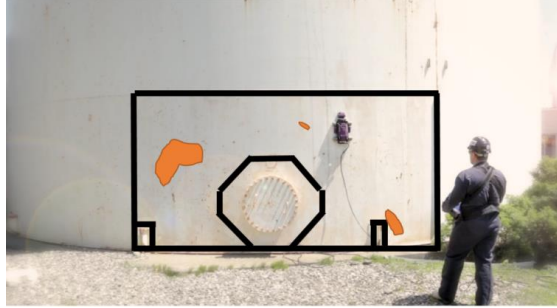

Fig. 2. An illustration of the project, proposing a crawler to automatically map the structure's geometry (black lines) and highlight the regions of significant wall loss (Orange regions). Note that the black solid lines indicate the detected welded regions used to map the structure key features.

B. Occupancy Grid Mapping

Occupancy Grid Maps (OGM) were introduced in the mid-1980s by Elfes and Moravec [7,8]. The mapping technique was developed to map an unknown and unstructured environment using an autonomous mobile robot, see Fig. 3 . The occupancy term is defined in the probability space that has two possible states of free and occupied. An occupancy grid map is then an array of occupancy variables. OGM algorithms usually incorporate a range sensor such as a 2D LiDAR sensor to provide occupancy probabilities based on the robot positions and the measurements. OGM algorithm requires to update the occupancy probability for each grid cell from the measurements in a Bayesian framework [9]. OGM eventually estimates the posterior probability over all grid cells of the map given the data. In order to avoid numerical instabilities, OGM is usually calculated in the log-odds form (logarithmical probability) as follows [9]:

$$l(m_i \,|z_{1:t}, x_{1:t}) = l(m_i \,|z_t, x_t) + l(m_i \,|z_{1:t-1}, x_{1:t-1}) \dots$$
$$-l(m_i), \qquad (1)$$

where $l(m_i \,|z_t, x_t)$, $l(m_i \,|z_{1:t-1}, x_{1:t-1})$ and $l(m_i)$ are the inverse sensor model, recursive term and the prior map respectively. m_i, $z_{1:t}$ and $x_{1:t}$ are a vector of grid cells, the set of measurements up to time step t and the set of all robot positions, respectively. The sensor model will be explained in section III. Note that the OGM algorithm requires the position of the robot consisting of x_r, y_r, θ_r, where x_r, y_r are position of the robot in the global coordinate, and θ_r is the robot's heading.

Fig. 3. An example of a mobile robot moving around to map the walls and obstacles of an experimental environment [10].

II. SIMULATION SETUP

The feasibility study was carried out by performing Finite Element Analysis (FEA) on PZFlex software (Onscale, CA, USA). FEA potentially gives rise to higher accuracy compared to other methods such as a ray-tracing modeling, at the expense of computation time.

An SH$_1$ wave mode with a 20 mm wavelength was excited on a 10 mm mild carbon steel sample with 20 meshes per wavelength, see Fig. 4. A square hole was designed in a flat plate to suggest a protruding welded tubular structure with a square hollow section (SHS), which is commonly used in offshore platforms [11]. Due to the high computational time of FEA in 3D, a small-scale concept-based laboratory size of a component was considered in the initial phase of this project.
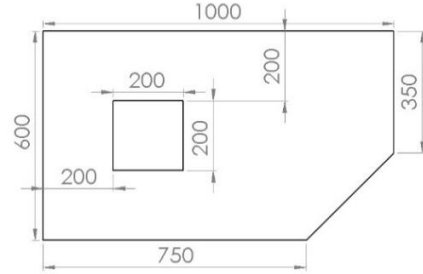

Fig. 4. Geometry of a carbon steel sample with a 10 mm thickness modelled in PZFlex software (top view), units are in mm.
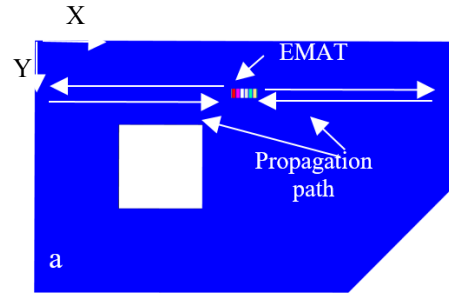

Fig. 5. Simulation of a PPM EMAT oriented in 0° direction in PZFlex software (top view). Note that measurements are carried out in three different wave propagation directions of 0°, 45° and 90°.

A six-row Periodic-Permanent-Magnet (PPM) EMAT generator was modelled in addition to two detectors on its left and right side, as shown in Fig. 5. An alternating in-plane loading is applied on each element in the ±Y direction. In-plane components of the signals reflected off the sample edges are then monitored in a pseudo pulse-echo mode. In general, separate

transmitter and receiver circuits are considered for optimizing the performance of both EMAT generator and detectors [12]. For the purpose of OGM, the Time of Flight (ToF) of the back-scattered signals are extracted by a cross correlation algorithm followed by a Hilbert transform.

III. METHODOLOGY

A Hanning-windowed sinusoidal tone burst signal with 7 cycles at the centre frequency of 227 kHz was chosen in order to excite the PPM EMAT, see Fig. 6. This frequency was selected in order to extend this research into defect identification in the future. The frequency was found to be suitable for identifying defects with a minimum depth of 50% thickness. The SH_1 wave mode disappears at this frequency for a 5 mm thick sample, meaning that this frequency can be used for identifying defects with a minimum depth of 50% of the thickness. Therefore, with this frequency, the OGM can be extended for the defect identification. The parameters used for calculating dispersion curves are summarised in Table I.

TABLE I.   MECHANICAL PROPERTIES OF THE SIMULATED SMAPLE

Density (kg/m³)	Longitudinal velocity (m/s)	Shear velocity(m/s)
7900	5900	3200

The predicted directivity pattern of the PPM EMAT confirms the bidirectional pattern of SH_1 wave mode, see Fig. 7. The directivity pattern was obtained by monitoring the amplitude of SH_1 wave modes at different angular positions around the transmitter in the far-field. Therefore, two EMAT detectors are considered in the measuring system in order to determine the true direction of each echo from each position. Fig. 8 illustrates the post-processed measured signals in a specific position of the robot using these two receivers. In order to correctly determine the ToFs, the measured signals from each detector are cross-correlated with the excitation signal and a Hilbert Transform was applied to obtain their ToF. It is important to note that a group velocity of 2159 m/s calculated by GUIGUW software [13] was considered for estimating the ranges.

In order to have an accurate sensor model for the OGM algorithm, the angular amplitude pattern of the PPM EMAT generator was calculated in PZFlex to determine the distribution value of occupied cells in the sensor model, as shown in Fig. 9.
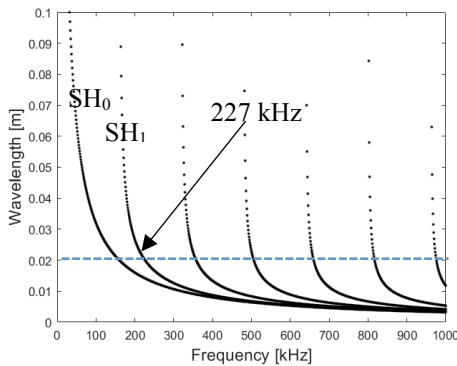
Fig. 6. Wavelength-frequency dispersion curve of the modelled sample calculated by GUIGUW software [13].
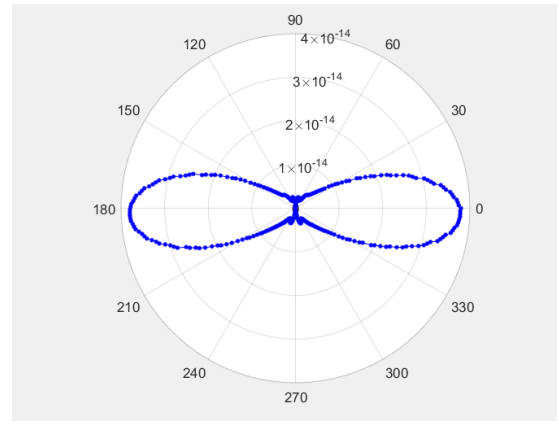
Fig. 7. Directivity pattern of the PPM EMAT measured at the far-field (75 mm from the PPM EMAT centre), showing the bidirectional propagation characteristics of the PPM EMAT at the excitation frequency of 227 kHz.
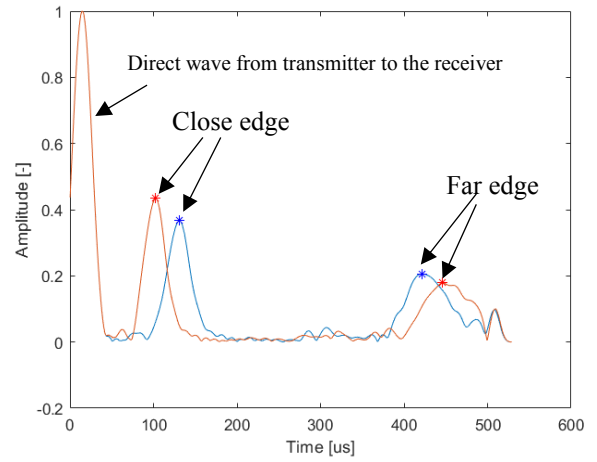
Fig. 8. Envelope of the cross-correlated signals measured in a specific position by two EMAT receivers in order to determine the direction of all echoes. Note that the first echo is disregarded as it is a direct wave from transmitter to the receiver.
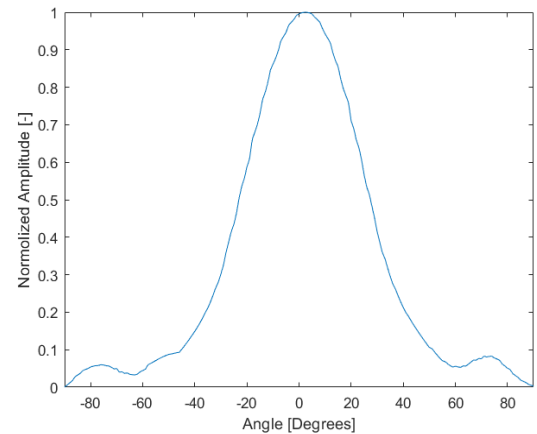
Fig. 9. Normalized amplitude of the EMAT generator as a function of angle measured at 227 kHz.

IV. RESULTS AND DISCUSSIONS

The simulated robot/EMAT positions are shown by the red arrows in Fig. 10. As the robot moves, the EMAT sensor mounted on the robot measures the new ToF ranges off the edges every five millimeters, and the OGM estimates the occupancy probability of each grid cell using the Bayesian filter, building the picture shown in Fig. 11. Overall, the correspondence of the ultrasonic mapping to the original structure is good. It was not possible to accurately map the corners and small features of the structure in addition to the presence of artifacts in the OGM. This is due to the wide divergence of the ultrasonic wave front and the acquisition of multiple reflections, causing variations in the ToF estimation. The goodness of fit is calculated as 0.78 between the estimated and the reference ranges using the Normalized Mean Square Error as the cost function. Note that the robot size and using a different number of EMAT and wave propagation orientations at each position may influence the reconstructed map obtained using an Occupancy Grid mapping technique.
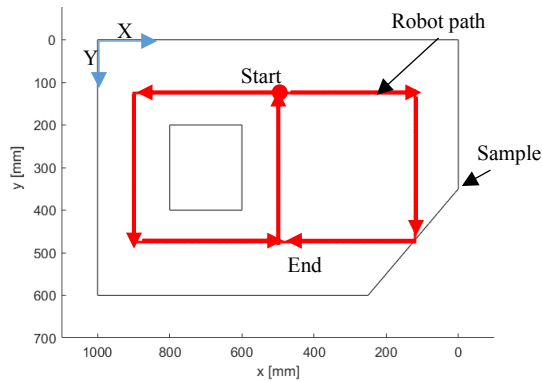

Fig. 10. The predetermined path of a robot to measure the signals across the samples (top view), EMAT generator is triggered every 5 milimeters on the path.
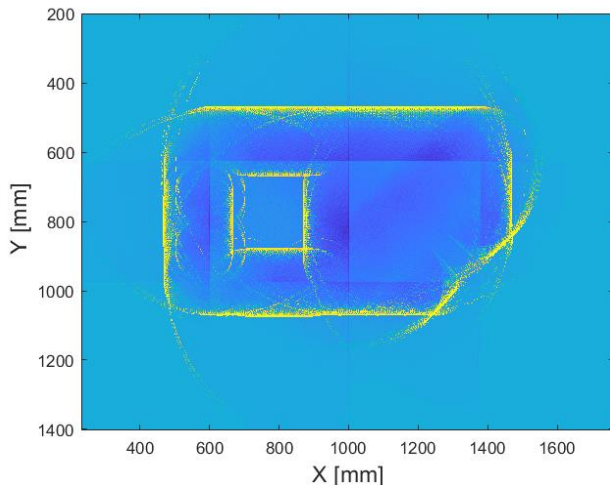

Fig. 11. Guided wave-based Occupancy grid mapping, illustrating that the technique is able to roughly estimate the geometry features of an unknown component. Note that signals are measured in three PPM EMAT directions (0°, 45°, 90°) in every measurement. Yellow points indicate the occupied cells.

In this paper, due to high computational time of the simulated data, only three EMAT directions of 0°, 45° and 90° were taken into account for the measurement at each robot position. In the future, experiments will be carried out to validate the simulation results using an Inuktun magnetic crawler (see Fig. 12) [14].
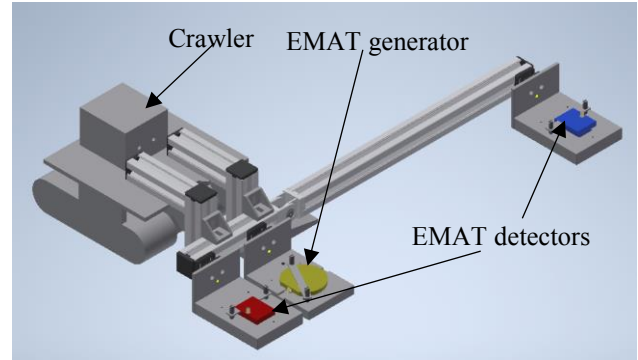

Fig. 12. EMAT trasnducers mounted on a crawler, a design for both pitch-catch and pseudo-pulse-echo measurments.

REFRENCES

[1] A. Khan, C. Mineo, G. Dobie, C. N. Macleod, and S. G. Pierce, "Introducing adaptive vision-guided robotic non-destructive inspection," in 46th Annual Review of Progress in Quantitative Nondestructive Evaluation, QNDE2019, July 14-19, 2019, Portland, OR, USA, 2019, pp. 1–4.

[2] "https://www.silverwingndt.com/scorpion2," Accessed Sept, 2019.

[3] Eddyfi UK Ltd, "Scorpion2 user's manual," 2005.

[4] S. E. Burrows, Y. Fan, and S. Dixon, "High temperature thickness measurements of stainless steel and low carbon steel using electromagnetic acoustic transducers," NDT&E Int., vol. 68, pp. 73–77, 2014.

[5] P. A. Petcher and S. Dixon, "Weld defect detection using PPM EMAT generated shear horizontal ultrasound," NDT&E Int., vol. 74, pp. 58–65, 2015.

[6] A. C. Kubrusly, M. A. Freitas, J. P. von der Weid, and S. Dixon, "Interaction of SH guided waves with wall thinning," NDT&E Int., vol. 101, no. October 2018, pp. 94–103, 2019.

[7] A. Elfes, "Sonar-Based Real-World Mapping and Navigation," IEEE J. Robot. Autom., vol. 3, no. 3, pp. 249–265, 1987.

[8] P. Moravec, "High Resolution Maps from Wide Angle Sonar," in IEEE international Conference on Robotics and Automation, 1985, vol. 2, pp. 116–121.

[9] S. Thrun, W. Burgard, and D. Fox, Probabilistic robotics. The MIT Press, 2006.

[10] E. Kaufman, K. Takami, T. Lee, and Z. Ai, "Autonomous Exploration with Exact Inverse Sensor Models," J. Intell. Robot. Syst. Theory Appl., vol. 92, no. 3–4, pp. 435–452, 2018.

[11] D. S. Saini, D. Karmakar, and S. Ray-Chaudhuri, "A review of stress concentration factors in tubular and non-tubular joints for design of offshore installations," J. Ocean Eng. Sci., vol. 1, no. 3, pp. 186–202, 2016.

[12] T. Kundu, Ultrasonic nondestructive evaluation–engineering and biological material characterization. CRC Press, Boca Raton, 2004.

[13] "http://www.guiguw.com/"

[14] "http://inuktun.com/en/products/onsite-standard-products/minitrac-crawler-track/, 2019.